Toxicon 220 (2022) 106955

Contents lists available at ScienceDirect

Toxicon

journal homepage: www.elsevier.com/locate/toxicon

Proteomics and histological assessment of an organotypic model of human skin following exposure to *Naja nigricollis* venom

Shirin Ahmadi [a,1], Spyridon T. Pachis [a,1], Konstantinos Kalogeropoulos [a], Farrell McGeoghan [a], Vahap Canbay [a], Steven R. Hall [b], Edouard P. Crittenden [b], Charlotte A. Dawson [b], Keirah E. Bartlett [b], José María Gutiérrez [c], Nicholas R. Casewell [b], Ulrich auf dem Keller [a], Andreas H. Laustsen [a,*]

[a] Department of Biotechnology and Biomedicine, Technical University of Denmark, Kongens Lyngby, Denmark
[b] Centre for Snakebite Research & Interventions, Liverpool School of Tropical Medicine, Pembroke Place, Liverpool, United Kingdom
[c] Instituto Clodomiro Picado, Facultad de Microbiología Universidad de Costa Rica, San José, Costa Rica

ARTICLE INFO

Handling editor: Dr. Denise Tambourgi

Keywords:
Snakebite envenoming
Naja nigricollis
Dermonecrosis
Skin organotypic
Shotgun proteomics
Pathway enrichment

ABSTRACT

Snakebite envenoming was reintroduced as a Category A Neglected Tropical Disease by the World Health Organization in 2017. Since then, increased attention has been directed towards this affliction and towards the development of a deeper understanding of how snake venoms exert their toxic effects and how antivenoms can counter them. However, most of our *in vivo* generated knowledge stems from the use of animal models which do not always accurately reflect how the pathogenic effects of snake venoms manifest in humans. Moreover, animal experiments are associated with pain, distress, and eventually animal sacrifice due to the toxic nature of snake venoms. Related to this, the implementation of the 3Rs principle (Replacement, Reduction, and Refinement) in the use of experimental animals in snakebite envenoming research is recommended by the World Health Organization. Therefore, more humane experimental designs and new *in vitro/ex vivo* alternatives for experimental animals are sought after. Here, we report the use of an organotypic model of human skin to further elucidate the pathophysiology of the dermonecrotic effects caused by the venom of the black-necked spitting cobra, *Naja nigricollis,* in humans. The goal of this study is to expand the repertoire of available models that can be used to study the local tissue damages induced by cytotoxic venoms.

1. Introduction

Snakebite envenoming is recognized as a Category A neglected tropical disease by the World Health Organization (WHO) (Chippaux, 2017). It is estimated that 1.8–2.7 million people are affected by snakebite envenoming annually, resulting in an estimated 81,000–238,000 deaths and 400,000 cases of permanent physical and psychological sequelae (Gutiérrez et al., 2017a). The clinical manifestations of snakebite envenoming include systemic complications, such as neurotoxic and hemotoxic effects, and local complications, such as tissue necrosis (Gutiérrez et al., 2017a). *Naja nigricollis*, the black-necked spitting cobra, is one of the most medically important snake species in Africa. Envenomings by *N. nigricollis* are characterized by severe cutaneous necrosis and, when venom is spat into the eyes, ophthalmic lesions (Habib and Gopalakrishnakone, 2013). This local tissue damage is likely mediated by cytotoxins (CTxs) which are the most abundant component in the venom of many cobra species (*Naja* spp.) (Petras et al., 2011). CTxs belong to the three-finger toxin (3FTx) family of proteins (Kessler et al., 2017), which interact with the phospholipid bilayer of membranes in various cell types, disrupting their integrity and inducing cytotoxicity associated with pore formation and cell lysis (Pucca et al., 2020). Although the timely administration of anivenoms containing animal-derived polyclonal antibodies (Gutiérrez et al., 2011) – the standard of care in snakebite envenoming cases – is generally effective at abrogating systemic toxicities, it largely fails to prevent the local tissue damage caused by *N. nigricollis* venom (Ho et al., 2021; Liu et al., 2020; Rivel et al., 2016). This is to a large extent due to the inherently low immunogenicity of CTxs, partially owing to their small size

* Corresponding author.
E-mail address: ahola@bio.dtu.dk (A.H. Laustsen).
[1] These authors contributed equally to this work.

https://doi.org/10.1016/j.toxicon.2022.106955
Received 22 August 2022; Received in revised form 3 October 2022; Accepted 16 October 2022
Available online 27 October 2022

(approximately 7 kDa) (Dufton and Hider, 1988). The discovery of more effective therapeutics against CTxs that would complement the action of antivenoms is thus imperative. However, to develop such therapeutics, it is crucial to better understand the mechanisms by which CTxs induce their cytotoxic damage.

Currently, murine models of envenoming are the gold standard for studying venom-induced pathologies *in vivo* (Gutiérrez et al., 2017b). Using murine models, it has been shown that venoms rich in CTxs cause dermonecrotic lesions (Rivel et al., 2016). However, the pathophysiology of venom-induced dermonecrosis observed in mice may not accurately mimic what takes place in human victims due to the differences in skin structure and function between mice and humans (Arnette et al., 2016a). Therefore, alternative models, that more closely resemble human skin tissue architecture, could be instrumental in elucidating the pathways that are involved in the pathological alterations induced by venoms in human skin. One such approach, likely to be of great value, is the application of organotypic models of human skin. These are three-dimensional (3D) cultures that enable higher degrees of architectural complexity and more accurately recapitulatate the spatial cell-cell or cell-extracellular matrix interactions than traditional monolayer (2D) cell cultures (Arnette et al., 2016b). Moreover, their use aids the reduction of experimental animals in research (Gutiérrez et al., 2020).

Here, we provide the first report of the use of an organotypic model of human skin to study the dermonecrotic effects of *N. nigricollis* venom, and the histological and proteomic observations made in this model were compared to an existing mouse model for context. Using this novel setup, we observe pathophysiological effects in the organotypic human skin model upon exposure to *N. nigricollis* venom which correlate to the more severe effects that are induced on a tissue level in the mouse model. In addition, our proteome analysis shows that widespread changes occur after *N. nigricollis* venom exposure in both the *in vitro* organotypic model and the *in vivo* mouse model. Meta-analysis of these datasets highlights a broad range of biological processes that are commonly affected in the two models and that follow what is known to occur upon skin damage and repair. Our work here introduces organotypic skin cultures as a potential model for the study of *N. nigricollis* venom-induced dermonecrosis and provides a new approach to study the biology of venom-induced pathophysiological effects.

2. Materials and methods

2.1. Monolayer cultures of human N/TERT keratinocytes and human dermal fibroblasts

N/TERT immortalized keratinocytes (kindly donated by Edel O'Toole from the Queen Mary University of London) were cultured as previously described (Pucca et al., 2020). Primary human dermal fibroblasts (Sigma-Aldrich, 106–05N) were cultured in Dulbecco's modified Eagle's medium/Nutrient mixture F-12 (DMEM/F-12; Gibco, 11320033) supplemented with 10% (v/v) fetal bovine serum (FBS; Fisher Scientific, 11550356), 1% (v/v) penicillin-streptomycin (Sigma-Aldrich, P4333), and 2 mM L-Glutamine (Gibco, 25030081) under standard mammalian cell culture conditions (37 °C, 5% CO_2, and 85% humidity). At approximately 80% confluency, the keratinocytes and fibroblasts were used for generating organotypic models of human skin.

2.2. Generating 3D organotypic models of human skin

Per organotypic culture, 60 μL Collagen I (Corning, 354236), 60 μL Matrigel (Corning 354234), 17 μL of 10 × Minimum Essential Medium (10x MEM; Gibco, 21430–020), 17 μL FBS (Fisher Scientific, 11550356), and 17 μL of fibroblast suspension (for a final density of 5×10^5 cells per mL of the mixture) were mixed. Subsequently, 170 μL of the collagen–fibroblast mixture was added to each well of a 12-well Transwell® plate (Corning, 3470). After gel polymerization for 1h at 37 °C, fibroblast culture medium was added, and the organotypics were incubated overnight (fibroblast pre-conditioning). The next day, the fibroblast culture medium was removed and 1×10^5 keratinocytes were seeded in the central area of the collagen–fibroblast mixture in each well. Thereafter, the cultures were incubated overnight in keratinocyte culture medium. Finally, the keratinocyte culture medium was removed from the insert and the cultures were lifted to the air-liquid interface and grown for an additional fifteen days in keratinocyte culture medium, which was renewed every other day.

2.3. Subjecting the organotypic models of human skin to N. nigricollis venom

At day 17 of culturing, two organotypics were punctured and injected with 20 μL phosphate-buffered saline (PBS, pH 7.4) using a 25 μL syringe (Hamilton, 84855) and were considered as controls. Two other organotypics were injected with 20 μL of 1.6 μg/μL Tanzanian *N. nigricollis* venom (purchased from Latoxan, Portes-Les-Valence, France) and these were considered the venom-subjected condition samples. The dose of venom was determined based on an unpublished pilot dose-determination experiment. The media were renewed and the organotypic models were incubated overnight. The next day, both the control and the venom-subjected organotypics were harvested for histological and proteomics analysis.

2.4. In vivo experiments of N. nigricollis envenoming in a mouse model

All animal experiments were conducted using protocols approved by the Animal Welfare and Ethical Review Boards of the Liverpool School of Tropical Medicine and the University of Liverpool. The experiments were performed in specific pathogen-free conditions under licensed approval (PPL #P58464F90) of the UK Home Office and in accordance with the Animal [Scientific Procedures] Act 1986 and institutional guidance on animal care. The experimental animals (18–20 g, male, CD-1 mice, Charles River, UK) were housed in groups of three, with environmental enrichment, water and food *ad libitum*, their health monitored daily during acclimatization, and the experimental design was based upon 3R-refined WHO-recommended protocols (Chippaux, 2010) with animals randomized. Experimental animals were briefly anesthetized using inhalational isoflurane (4% for induction of anesthesia, 1.5–2% for maintenance) and intradermally injected in the shaved rear quadrant on the dorsal side of the flank skin with either 31.5 μg (low dose; n = 3) or 63 μg (high dose; n = 3) of Tanzanian *N. nigricollis* venom (purchased from Latoxan, Portes-Les-Valence, France) dissolved in 50 μL of PBS. The mice were observed three times daily up to 72h post-injection to ensure wellbeing and that there were no signs of systemic envenoming. After 72h, experimental animals were euthanized using increasing concentrations of CO_2, after which the skin surrounding the injection site was dissected and internal skin lesion sizes measured in two directions with callipers and photographed. Cross-sections of the skin lesions and healthy skin control (collected from the opposite flank of the same animals) were further dissected and preserved in formalin fixative for routine tissue processing and mounted on microscopy slides for downstream histopathological analysis. In addition, biopsies of necrotic and healthy skin tissue from each animal were collected and stored at −80 °C for downstream proteomics analysis.

2.5. Histological analysis

Mouse skin samples underwent tissue processing using a Tissue-Tek VIP (vacuum infiltration processor) overnight, while the harvested organotypic models were fixed in 4% paraformaldehyde and routinely processed for histological analysis before being embedded in paraffin (Ultraplast premium embedding medium, Solmedia, WAX060). 4 μm paraffin sections were cut on a Leica RM2125 RT microtome, floated on a waterbath and placed on color slides (Solmedia, MSS54511YW) or

poly-lysine slides (Solmedia, MSS61012S) to dry. For haematoxylin and eosin (H&E) staining, slides were deparaffinized in xylene and rehydrated in decreasing grades of ethanol (100%, 96%, 85%, 70%) to distilled water before being stained in haematoxylin for 5 min, "blued" in tap water for 5 min, and stained in eosin for 2 min. Slides were then dehydrated through 96% and 100% ethanol to xylene and cover slipped using DPX (Cellpath, SEA-1304-00A). Haematoxylin (Atom Scientific, RRBD61-X) and Eosin (TCS, HS250) solutions were prepared in-house.

For immunohistochemical analysis, the organotypic sections were deparaffinized in two changes of xylene for five and 3 min, respectively, then re-hydrated in decreasing grades of ethanol (100% twice, 90%, 80%, and 70%) for 3 min each. Sections were washed in phosphate-buffered saline (PBS) for 5 min, then blocked by incubating in a buffer consisting of 1% bovine serum albumin (BSA) w/v, 2% fetal bovine serum (FBS) v/v in PBS, and additionally containing 5–10% goat serum (Sigma) for 1 h at room temperature. Sections were then probed with primary antibody diluted in PBS containing 1% BSA and incubated on the section at room temperature for 2 h or overnight at 4 °C, staining for cytokeratin 1 (ab93652; Abcam), cytokeratin 14 (ab7800; Abcam), integrin alpha 6 (ab181551; Abcam), or involucrin (ab181980; Abcam). Sections were washed three times with PBS before addition of the secondary antibody, goat Alexa Fluor 488-green (ab150113; Abcam) or 568-red (ab175471; Abcam), at a 1:500 dilution for 1 h at room temperature. Sections were washed three times in PBS before 4′,6-Diamidino (Chippaux, 2017)2-phenylindole (DAPI; D9542; Sigma-Aldrich) at a 1:1000 dilution was used as a nuclear stain. Following a further three washes in PBS the sections were mounted using Epredia Immu-mount (Fisher Scientific; 10622689). Transmission light and immunofluorescence microscopy imaging was performed with an Invitrogen Evos FL Auto 2 microscope using a 20x or 60x magnification lens. Acquired images were further analyzed in Fiji (Schindelin et al., 2012), and stitching was performed using a plugin developed by Preibisch et al. (Preibisch et al., 2009).

2.6. Proteomics

Two-to-three mg of the organotypic models and mouse skin samples (both controls and venom-subjected samples) were placed into Pressure Cycling Technology (PCT) microtubes containing 30 μL of 4 M guanidine hydrochloride and homogenized in a Barocycler (Pressure Biosciences, Inc) for 60 cycles of 20 s at 45 kpsi and 10 s at atmospheric pressure, at 33 °C. The homogenates were reduced and alkylated by adding 1 μL of 400 mM tris(2-carboxyethyl)phosphine (TCEP) and 3 μL of 200 mM chloroacetamide (CAA) and incubated for 30 min at ambient temperature with 600 rpm shaking. The samples were digested using Lys-C at a ratio of 1:100 Lys-C:Protein (w:w), with the microtubes placed into the Barocycler for 45 cycles of 50 s at 20 kpsi and 10 s at atmospheric pressure, at 37 °C. After that, trypsin was added at a ratio of 1:20 trypsin: protein (w:w), and the microtubes were placed back into the Barocycler for 90 cycles of 50 s at 20 kpsi and 10 s at atmospheric pressure, at 37 °C. Digestion was stopped by acidifying with 10% trifluoroacetic acid (TFA) for a final concentration of 1%. The digests were desalted using tips packed with Empore C18 discs (ThermoFisher Scientific, 13-110-019) with approximately 5–10 μg/plug peptide capacity. The C18 membrane was activated with 100% methanol (MeOH), and equilibrated with 0.1% formic acid (FA). The samples were loaded onto the column, washed twice with 0.1% FA, and then eluted in 80% acetonitrile (ACN) containing 0.1% TFA. The eluate was dried under vacuum at 30 °C, re-suspended in LC–MS buffer (2% ACN, 1% TFA), and the peptide concentration was determined using a NanoDrop One Spectrophotometer (ThermoFisher Scientific).

Mass spectrometry data were collected using a Q Exactive mass spectrometer (ThermoFisher Scientific, San Jose, CA) coupled to a Proxeon EASY-nLC 1200 liquid chromatography (LC) system (ThermoFisher Scientific). Peptides were separated for 140 min on a 50 cm × 75 μm microcapillary PepMap RSLC C18 resin (2 μm, ThermoFisher Scientific, TF164711), packed inside an EasySpray ES803A column. For analysis, 500 ng of samples were loaded onto the analytical column. Full MS spectra were collected at a resolution of 70,000, with an AGC target of 3×10^6 or a maximum injection time of 20 ms and a scan range of 300–1750 m/z. The MS2 spectra were obtained with a top 10 method at a resolution of 17,500, with an AGC target value of 1×10^6 or maximum injection time of 60 ms, normalized collision energy of 25, and an intensity threshold of 1×10^3. Dynamic exclusion was set to 45 s, and ions with a charge state 1 were filtered out. The gradient started with 10% buffer B (80% ACN with 0.1% FA) and increased to 23% buffer B in 85 min. It further increased to 38% buffer B in 30 min, before finally going to 60% buffer B in 10 min. A washing step with 95% buffer B was then performed for 15 min. Mobile phase buffer A contained ultra-pure H_2O with 0.1% FA.

The raw data obtained from the analysis of the organotypic samples were searched with Proteome Discoverer 2.5 software. The Sequest engine was used for assigning spectra to peptides, with human proteins included as the target database (reviewed human proteome database was downloaded from UniProt, accessed September 14th, 2017, 42,157 sequences). Precursor tolerance was set to 10 ppm, and fragment mass tolerance was set to 0.02 Da. Peptide minimum length was set to 6 residues, while maximum length was 144. Carbamidomethylation of cysteines (+57.021 Da) was added as static modification, while methionine oxidation (+15.995) and the protein N-terminal modifications, namely acetylation (+42.011), methionine loss (−131.040 Da), and methionine loss plus acetylation (−89.030 Da) were included as variable modifications. Only b and y fragment ions were considered for precursor identification. False Discovery Rate (FDR) was controlled with the Percolator node, and protein and peptide target FDRs were set to 1% and 5% for strict and relaxed targets, respectively. For label-free quantification, the Minora Feature Detector node was added in the processing workflow, and the Feature Mapper and Precursor Ions Quantifier were added in the consensus workflow. Unique and razor peptides were considered for protein quantification, and normalization mode was set to total peptide amount. All other node settings were set to default values. The raw data from mouse samples were searched with the same settings, with the exception of the FASTA database used in the Sequest node, which was set to the mouse UniProt proteome (reviewed murine proteome database was downloaded from UniProt, accessed September 9th, 2020, 25,101 sequences). Search results were exported for further processing.

2.7. Proteomics data processing, statistics, and analysis

Protein abundance data collected from the mass spectrometry experiments on the organotypic skin models and mice were first filtered so that only proteins that were present in at least two out of three replicates in the mouse samples or in both replicates in the case of the organotypic models, which only had two replicates in each condition (control or venom-subjected), were considered for further processing. Proteins that met these criteria in one condition, but were completely absent in the other condition, were also included in the analysis. Principal component analysis was performed using ClustVis (Metsalu and Vilo, 2015), a web tool found at https://biit.cs.ut.ee/clustvis/. Further processing took place as described by Aguilan et al. (2020) to identify proteins significantly decreased or increased in abundance in the venom-subjected condition compared to control as reflected by the fold-change and associated p value calculations of protein abundances. In brief, abundance values were transformed into their $\log_2$ equivalents and underwent two types of normalization. In the first, each value was scaled against the average of all protein abundances in the specific sample. In the second, values were normalized by their distribution width, which corrects for potential differences in the dynamic range of acquisition between samples. The Probabilistic Minimum Imputation model, which assumes low abundance resampling, was used to impute missing values. Low abundance was intended as >2 standard deviations smaller than the

distribution of all valid values, and the resampling variability was set to 0.3. The fold-change was calculated as the ratio of transformed and normalized protein abundance values between the venom-subjected condition and controls. *P* values were calculated by performing different t-tests depending on whether the replicates for each protein were homoscedastic or heteroscedastic as determined by F-tests. Volcano plots and other graphs were created in Prism v.9 (GraphPad). Pathway enrichment analysis was performed by feeding the lists of significantly affected proteins in the venom-subjected condition compared to the controls through the online Metascape tool (Zhou et al., 2019). The occurring interaction network clusters were further visualized and edited in Cytoscape (Shannon et al., 2003).

3. Results

3.1. Establishment of the organotypic models of human skin

Organotypic models of human skin were established according to a 16-day cell culturing scheme (Fig. 1a). On day 17, the organotypic models were punctured and injected either with PBS, as a control, or with 32 μg of *N. nigricollis* venom, and were harvested 24 h later. It is worth highlighting that the 24 h endpoint of the exposure to the snake venom deviates from the 72 h standard time for assessing dermonecrosis in mouse models. This was due to issues relating to the liquid cultures, in which the organotypic models are maintained, namely the requirement to renew the cell culture medium every other day – a requirement made even stronger by the accumulation of cell debris due to the cytotoxic action of the venom. The medium renewal that would have been required to extend the incubation time to 72 h could have interfered with the experiments in ways that are difficult to control. Therefore, in this study we chose to focus on the acute effects and responses that could be observed after 24 h.

As previously reported, contraction of the collagen-fibroblast matrix was observed in the organotypics, indicating successful establishment of the dermal layer (El-Ghalbzouri et al., 2002). Various degrees of contraction were observed between the individual organotypic models (Fig. 1b).

Microscopic imaging of the organotypic sections revealed a cellular organization comparable to that of human skin. A single row of mitotically active, columnar, or cuboidal cells, *i.e.*, stratum basale (SB) (Petrova et al., 2014) of epidermis, could be seen on top of the collagen-fibroblast matrix (Fig. 1c). Upwards, the stratum spinosum (SS), comprising 4–5 layers of polyhedral keratinocytes, was observed. The SS keratinocytes produce significant amounts of desmosomes, anchoring the cells to each other. Notably, dehydration of the organotypic models, during fixation, slightly shrank the SS keratinocytes, but they remained tightly bound to each other through the desmosomes (Yousef et al., 2021) (Fig. 1c, red arrow heads). In some of the sections, but not all, a thin layer of granular keratinocytes, the stratum granulosum (SG), was seen on top of the SS layer. Moving upwards, the SG keratinocytes usually lose their nuclei and organelles, turning into corneocytes. The corneocytes, in turn, form the stratum corneum (SC), which is the outermost layer of intact skin (Yousef et al., 2021). The SC performs a crucial barrier function that prevents the penetration of external compounds into the body. The SC was not observable in the H&E-stained sections, most likely as an artefact of the sample preparation procedure. However, cytokeratin 1 (suprabasal keratinocyte marker), cytokeratin 14 (a protein isoform that is highly expressed in basal cells), involucrin (late differentiation marker), and integrin alpha 6 (marker of basal epithelial cells in contact with the basement membrane) immunostainings confirmed the presence of differentiated layers of stratified epithelium in the organotypic models (Dyring-Andersen et al., 2020; Sanz-Gómez et al., 2020). Overall, the histological analysis of the cross-sections demonstrated differentiated layers of epidermal cells and confirmed the successful establishment of the organotypic models of human skin.

3.2. Histopathological effects of N. nigricollis venom on mouse skin and organotypic models of human skin

Mice (n = 3 per group) received flank injections with either 31.5 μg (low dose) or 63 μg (high dose) of *N. nigricollis* venom with lesions dissected post-euthanasia 72h later. The non-injected flank on the opposite side of each mouse was used as a healthy internal control. Although both groups of venom-injected mice developed skin lesions, the lesion area was not significantly different between the low and high venom dose groups. Notably, in both groups, the lesion area in one animal was considerably different than the other two (Figure S1a). For the remainder of this study, all mentions of experiments and analyses involving mouse samples refer to the animals that received the high dose of venom (63 μg).

A healthy macroscopic (Figure S1b) and microscopic (Fig. 2a, left panel) appearance of inner skin was seen in the control flanks of mice. Focusing on the epidermis of the control skin, two-to-three layers of intact keratinocytes could be seen (Fig. 2a, right panel zoom-in). In contrast, macroscopic lesions (Figure S1c) defined by histological alterations ranging from mild (Fig. 2b, left panel) to more severe (Fig. 2c, left panel) were observed in the flanks injected with *N. nigricollis* venom. These alterations included (i) thickening of the epidermal layer due to hyper-proliferation and aberrant differentiation of keratinocytes (hyperplasia), (ii) emergence of proteinaceous material, which forms a sheet overlying the keratinocytes, and (iii) loss of the continuity of the epidermis, *i.e.*, epidermal disappearance. Epidermal hyperplasia, which generally is seen during mild inflammatory responses to wounding, was the most frequently observed alteration in the cross-sections (Fig. 2b, right panel zoom-in). In comparison, a necrotic scar, which is identified by the presence of a proteinaceous material (Fig. 2c, right panel zoom-in) and discontinuity of the epidermis, was seen in a minority of the sections.

The constituted organotypic models of human skin were also subjected to punctures and injections with either PBS, as a control, or 32 μg of *N. nigricollis* venom. A comparison of the control and venom-injected samples from mice with the organotypic models of human skin highlights considerable differences between the two models under the control condition, but also notable similarities under the venom-subjected condition. Skin epidermis in mice contains only two to three layers of keratinocytes (Fig. 2a, right panel zoom-in), while the control organotypic model, similarly to intact human skin, is comprised of multiple layers of differentiated keratinocytes, resulting in a thicker epidermis (Fig. 2d) (Salgado et al., 2017). Similar to the more drastic alterations seen in some of the slices of venom-treated mouse skin, keratinocytes of the venom-injected organotypic models demonstrated clear signs of necrosis, resulting in markedly fewer live cells. In addition, the well-defined organization of the keratinocyte layers was lost (Fig. 2e).

In summary, the organotypic human skin model recapitulates the differences in epidermis organization that are observed in healthy tissue between humans and mice. Exposure to *N. nigricollis* venom led to several pathological alterations of varying severity in the skin of mice, while in the organotypic models, the more severe necrotic phenotypes were predominantly observed. A plausible explanation for this could be that the small size of the organotypic models resulted in the majority of the cells becoming exposed to venom toxins. The liquid culture in which the organotypic models are incubated could further promote the equal distribution of the venom toxins.

3.3. Exposure to N. nigricollis venom leads to extensive alterations in the proteomic landscape of mouse skin and the organotypic model of human skin

To examine the global proteome effects that accompany the pathological alterations observed and described above, we employed a shotgun proteomics approach for identification of the proteins present in the samples and their abundance. After filtering of the detected proteins,

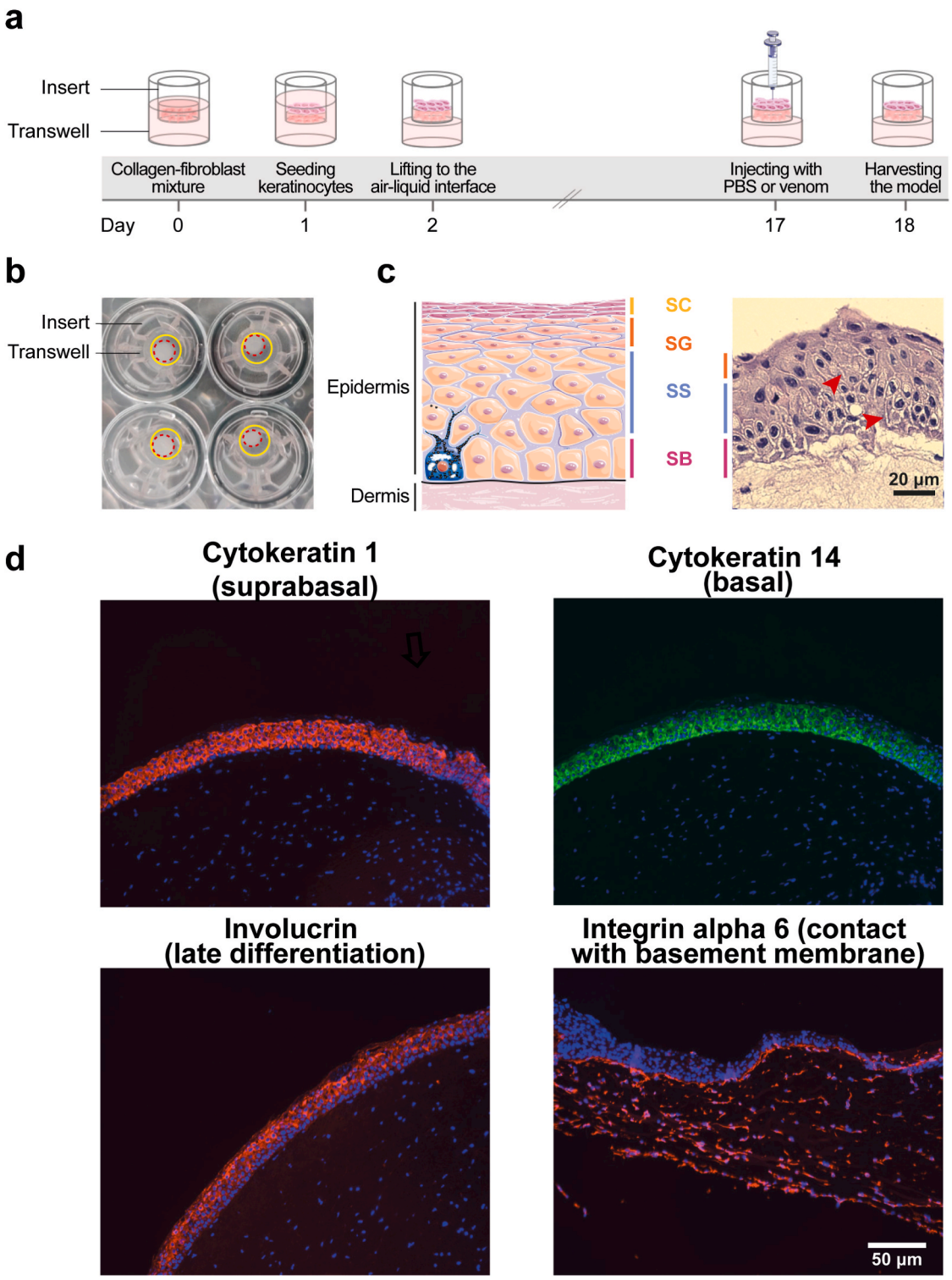

Fig. 1. Establishing an organotypic model of human skin. **(a)** Cell culture protocol. A collagen-fibroblast matrix was incubated overnight in fibroblast culture medium (added to both the Transwell and the Insert). Keratinocytes were seeded onto the collagen–fibroblast matrix and were kept submerged in keratinocyte culture medium (added to both the Transwell and the Insert). Organotypic rafts were raised to the air–liquid interface, with keratinocyte culture medium only being added to the Transwell. After 2 weeks of growth at the air–liquid interface, the organotypic models were injected with either PBS or *N. nigricollis* venom. **(b)** Contraction of the matrix. Yellow circles demonstrate the original area occupied by the collagen–fibroblast matrix before contraction, and the dotted red lines show the matrix area after contraction. **(c)** Schematic illustration of human skin (left) and a comparison with the cellular organization of a representative histological section of an organotypic model stained with H&E (right). Different colors are used to annotate the various skin layers in the 2 panels. SC: stratum corneum; SG: stratum granulosum; SS: stratum spinosum; SB: stratum basale. Note that in the organotypic section, the SC is absent, and the SS is thinner compared to the schematic illustration. Red arrowheads point to desmosomes that connect the keratinocytes. **(d)** Cytokeratin 1 (red), cytokeratin 14 (green), involucrin (red), and integrin alpha 6 (red) immunostainings confirm the presence of differentiated keratinocytes, including the skin barrier (*i.e.*, stratum corneum). Cell nuclei are stained with DAPI (blue) in all images. For interpretation of the references to color in this figure legend, the reader is referred to the Web version of this article.

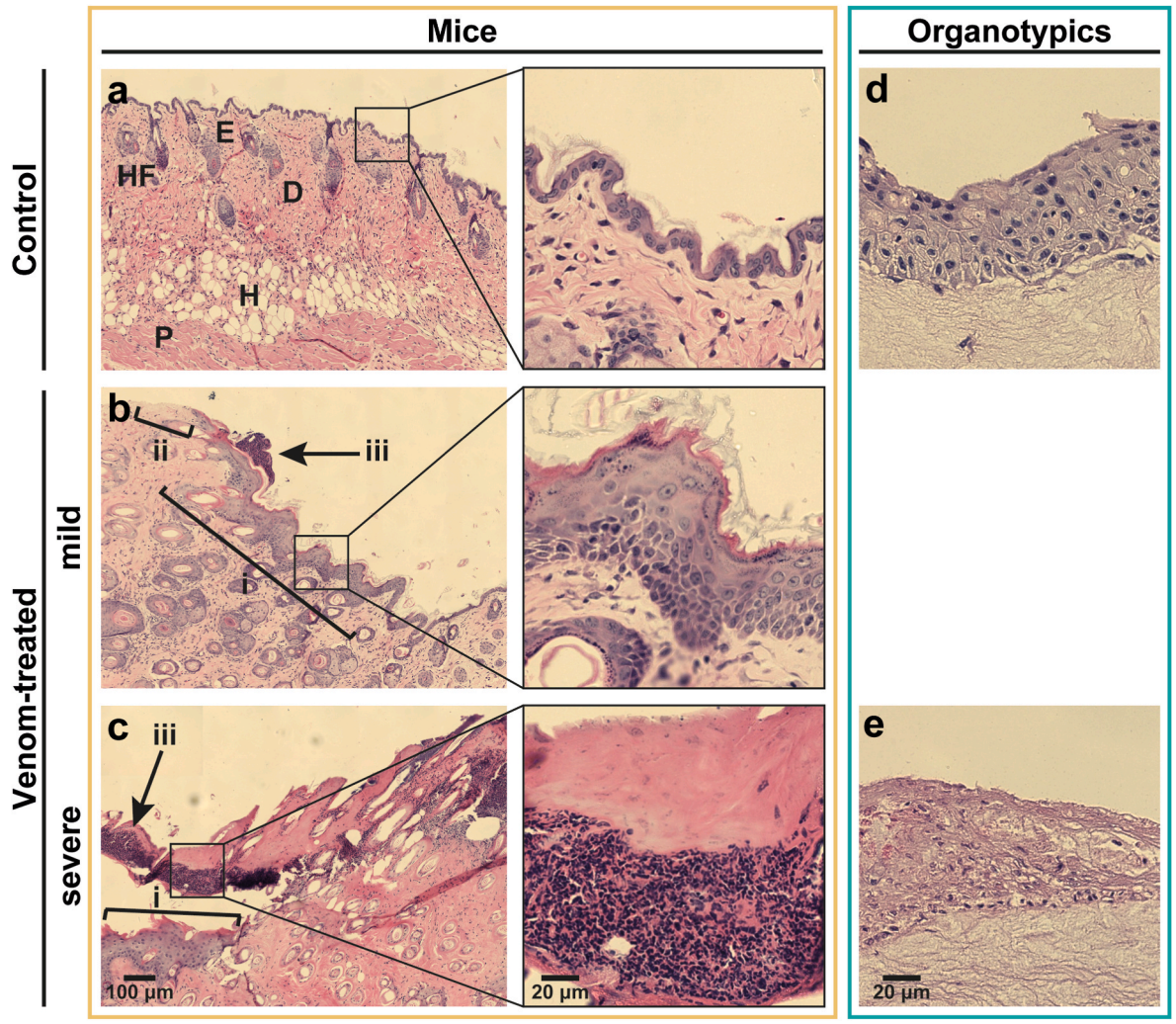

Fig. 2. *Naja nigricollis* venom injections in mice and organotypic human skin models lead to a range of histological alterations. **(a)** Left panel: Light micrograph of H&E-stained control mouse skin demonstrates the characteristic histological pattern, with the epidermis (E), the dermis (D), hair follicles (HF), the hypodermis (H), and the Panniculus carnosus (P) annotated in capital letters. Right panel zoom-in: Control mouse epidermis displays 2–3 continuous layers of keratinocytes. **(b)** Left panel: Mild alterations of mouse skin in response to the venom injections. The epidermal hyperplasia (i), epidermal discontinuity (ii), and proteinaceous material (iii) indicate a necrotic response. Right panel zoom-in: Epidermal hyperplasia. **(c)** Left panel: Severe alterations of mouse skin in response to the venom injections. Epidermal hyperplasia (i) and a very prominent proteinaceous material (iii) can be seen here, too. Right panel zoom-in: Proteinaceous material of the necrotic region. **(d)** Multi-layer keratinocyte organization in the human skin organotypic model under control conditions. **(e)** Extensive keratinocyte cell death due to exposure to venom in the human skin organotypic model.

2498 proteins remained and were taken along for further analysis in the mouse sample dataset, while this number was significantly lower in the organotypics, with 1301 proteins being further analyzed. 924 proteins were found in both datasets, constituting approximately 37% and 71% of the total pool of proteins in the proteomics of the mice and organotypic models, respectively (Fig. 3a). The detected proteins underwent a series of transformation and normalization steps in order to go from the mass spectrometry's intensity output values (corresponding to protein abundances) to the fold-changes in abundance for each protein between the control and venom-subjected conditions (Tables S1 & S2) (Aguilan et al., 2020).

Principal component analysis was carried out using the normalized proteomic profiles of the individual replicates in each condition in order to compare their similarity. For the most part, the control replicates clustered together and away from the venom-subjected replicates in both datasets as expected (Fig. 2b). However, the venom-subjected replicates did not all cluster together, indicating that the venom injections had variable effects on a proteomic level between animals. It is also worth noting that venom-subjected replicate #2 in the mouse dataset clustered closely with control replicate #1, suggesting that the region of the lesion that was used for the proteomics experiments showed few protein abundance alterations in response to the venom exposure in this animal. A plausible explanation for this observation is proposed in the Discussion section below.

An overview of the fold changes, visualized as the ratio of each protein's abundance in the venom-subjected condition over the control, and plotted against their p values (statistical significance) can be seen in Fig. 3c. Proteins whose abundance is significantly altered (2-fold decreased or increased in the untransformed dataset) and is accompanied by high statistical confidence (raw p value < 0.05) can be seen annotated in color. A significant decrease in the abundance of 118 proteins was observed when mice were challenged with venom (purple dots), whereas 134 proteins were more abundant (orange dots). In the organotypic models, the abundance of 104 proteins was significantly decreased, while it was significantly increased for 124 proteins. When the lists of significantly affected proteins were compared between models, only a few proteins were found in common. Phosphohistidine phosphatase 1 (PHPT1) was the only protein found to be significantly

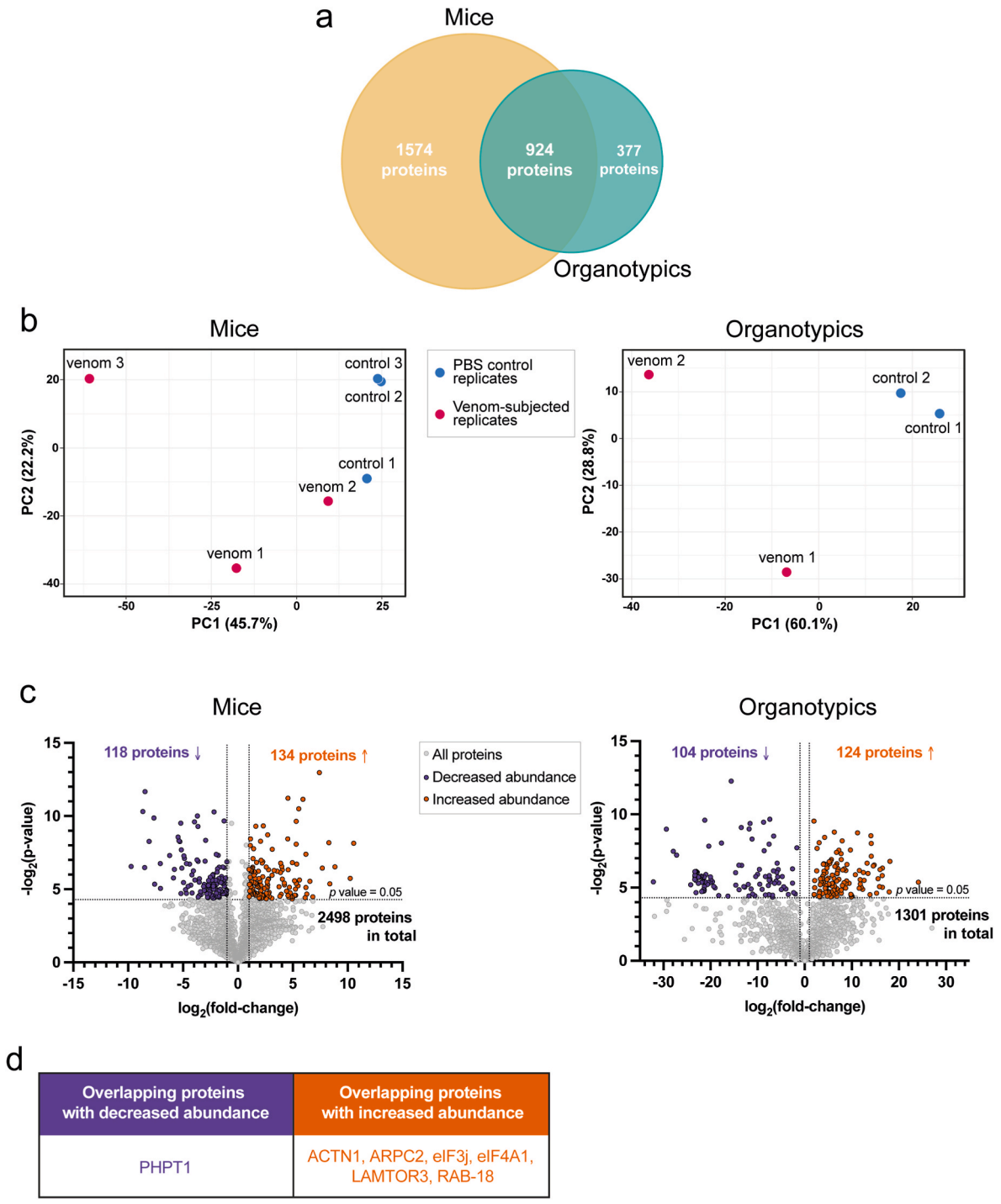

Overlapping proteins with decreased abundance	Overlapping proteins with increased abundance
PHPT1	ACTN1, ARPC2, eIF3j, eIF4A1, LAMTOR3, RAB-18

Fig. 3. Shotgun proteomics on mouse skin and organotypic models subjected to *N. nigricollis* venom. **(a)** Venn diagram depicting the proteins found in common between the mouse and organotypic model datasets. **(b)** Principal component analysis depicting the similarity between replicates (control and venom-subjected) in each model. In the mouse dataset, the first and second principal component cumulatively explain 67.9% of the variance observed, while in the organotypic model dataset, they explain 88.9% of the variance. Control replicates are annotated as blue dots, while venom-subjected replicates are annotated as red dots. **(c)** Volcano plots of all detected proteins (grey dots) in mouse and organotypic model samples after filtering, transformation, and normalization steps. The log2 value of the fold-change in protein abundance between venom-subjected and control conditions is plotted on the x-axis, while the -log2 value of the corresponding *p* value (statistical significance) is plotted on the y axis. Each dot represents a single protein. Proteins with a log2(fold-change) value < -1 or >1 (2-fold decrease or increase in abundance in the untransformed dataset) and a -log2(*p* value) > 4.32 (raw *p* value < 0.05) are annotated in color as significantly affected. Decreased abundance proteins are seen in purple and increased abundance proteins in orange. **(d)** Table depicting the proteins found in common between the lists of significantly affected proteins in the two models. For interpretation of the references to color in this figure legend, the reader is referred to the Web version of this article.

less abundant in the venom-subjected condition. It has been previously shown that PHPT1 overexpression in primary neurons decreases cell viability (Krieglstein et al., 2008). On the other hand, alpha actinin 1 (ACTN1), actin-related protein 2/3 complex subunit 2 (ARPC2), eukaryotic translation initiation factor 3 subunit J (eIF3j), eukaryotic translation initiation factor 4A-1 (eIF4A1), late endosomal/lysosomal adaptor and mitogen activated protein kinase and mechanistic target of rapamycin activator 3 (LAMTOR3), and Ras-related protein RAB-18 were found in the increased abundance list. These proteins are involved in cell-matrix adhesion organization in keratinocytes (Hamill et al., 2015), cytoskeleton regulation and re-organization (Choi et al., 2019), translation (Zhao et al., 2020), cell growth signaling (Sancak et al., 2010), and vesicle trafficking (Filipek et al., 2017; Li et al., 2017).

To summarize, the proteomes of mouse skin and the human skin organotypic models under control and venom-subjected conditions were analyzed. Overall, we found that the proteomes in the two models showed a large overlap, at least quantitatively (i.e., which proteins were present). We also observed that the venom injections led to a variable proteomic profile in both models, and while the numbers of proteins with significantly decreased and increased abundance were similar between the two models, the overlap of identical proteins in these lists is limited.

3.4. Pathway enrichment analysis highlights commonalities in the venom-affected pathways between the mouse skin and organotypic human skin models

We next wanted to examine whether exposure to *N. nigricollis* venom resulted in specific pathways being commonly affected in the two models. For this, a pathway enrichment analysis was performed with the Metascape web tool (Zhou et al., 2019), using the lists of significantly affected proteins that were previously obtained. Metascape incorporates a core set of default ontologies for enrichment analysis in its pipeline, including GO processes, KEGG pathways, and Reactome gene sets among others. This was performed separately for proteins whose abundance was significantly decreased and increased, respectively. Indeed, more potentially biologically relevant connections between the two models were observed when also looking at proteins of each dataset that are not identical to proteins of the other but are both members of the same gene ontology terms (Fig. 4a). This observation was more pronounced for the proteins whose abundance was significantly increased.

The top 20 enriched terms across the protein lists (significantly decreased and increased, respectively) from both models were depicted as heatmaps, color-coded based on their p value (Fig. 4b). These terms covered a broad range of biological processes and signaling pathways. The enriched pathways relating to the decreased abundance proteins showed very little overlap between the two models and were often associated with general metabolism-related processes (Fig. 4b left panel). On the other hand, the enriched pathways associated with the increased abundance proteins displayed a much higher overlap between the two models and were generally involved in cellular processes, such as regulation of actin cytoskeleton, Rho GTPases signaling, apoptosis, and the regulation of expression of SLITs and ROBOs (Fig. 4b right panel). It is worth noting that the enriched terms that were only associated to the increased abundance proteins derived from the mouse dataset were mostly associated with humoral immune and acute inflammatory responses triggered by the damaged tissue. A complete overview of the enriched terms that came out of each list in the Metascape analysis can be found in Table S3.

Going forward, analysis was only continued for the data relating to the increased abundance proteins, as these exhibited a higher overlap between the two models in enriched terms related to skin homeostasis and wounding. Next, the pooled datasets from the two models were used to visualize all the known protein interactions, as this could highlight additional pathways that are potentially affected by venom toxins. A highly complex interactome network was constructed (Fig. 4c), which could be used to parse out specific clusters corresponding to protein complexes (Fig. 4d). Some of the interesting clusters that appeared contained members from both datasets (red vs blue dots), and these individual clusters were tested for enriched ontology terms. The results indicated that an upregulation of processes relating to the formation of the cornified envelope/keratinization, insulin-like growth factor (IGF) signaling, and phosphatidylinositol 3-kinase/protein kinase B (PI3K-Akt) signaling took place, among others.

Lastly, the presence of certain other potentially interesting groups of proteins in the obtained proteomics datasets was investigated. The first group consisted of damage-associated molecular pattern molecules (DAMPs). These are proteins that have been described to be abundant in wound exudates collected from mice exposed to viperid venom, and are involved in the pathophysiology observed upon envenoming (Rucavado et al., 2016). The second group consisted of proteins involved in chemokine/cytokine signaling as we predicted that the arrival of immune cells to the site of injury would more strongly mediate an inflammatory response in mice. Overall, proteins from both aforementioned groups were found in our datasets (green dots for DAMPs, pink dots for chemokines/cytokines) (Figure S2a). While the majority of DAMPs detected appeared to have some abundance alterations in both datasets, only a few that were present in the mouse dataset were deemed statistically significant (p value < 0.05). As for chemokines and cytokines, most of them were indeed present in the mouse dataset as predicted, and although they did seem to display increased abundance, most did not meet the significance criteria. The complete list of proteins of each group for the two models can be found in Table S4.

Our data showed that there is a much higher overlap between the lists of proteins whose abundance is significantly affected when examining them for non-identical proteins that are both members of the same gene ontology terms. This indicates that while there are not many identical proteins affected in the two datasets upon exposure to venom, many of the affected pathways and processes are likely common. Several upregulated signaling pathways were extracted from the list of proteins with significantly increased abundance, and these results were complemented and further expanded by looking at protein interactions and the complexes they form.

4. Discussion

Dermonecrosis is one of the main clinical manifestations of envenomings by *N. nigricollis* and other spitting cobras (World Health Organization, 2010), which together with other snakes are responsible for approximately 6000–15,000 annual snakebite-related amputations in sub-Saharan Africa (Chippaux, 2011). In part, these high numbers of severe venom-induced morbidity are the result of the inefficacy of current snakebite antivenoms at preventing cytotoxic pathophysiology and to limitations in the timely access to health facilities. Therefore, establishment of a new model to study snakebite-induced dermonecrosis is warranted in order to better characterize this relevant pathological effect. This study aimed to expand the repertoire of available models that can be used to study the necrotic effects of snake venoms by introducing the application of an organotypic model of human skin. This model was employed to study *N. nigricollis* venom-induced dermonecrosis from a histological and proteomic perspective in comparison to a more established *in vivo* mouse model. However, inherent differences between the *in vitro* organotypic model of human skin and the *in vivo* mouse model impose clear limitations in the direct comparison of the two models, which are discussed in detail below. Our goal was therefore not to assess whether skin organotypics can act as surrogates to mouse models, but rather to use the more established mouse model as a reference for investigating the potential value of the organotypic model as a tool in these types of studies.

The mouse skin and the organotypic models of human skin presented both similarities and differences. In terms of the histological pattern of epidermis, the organotypic model better resembles the human skin than

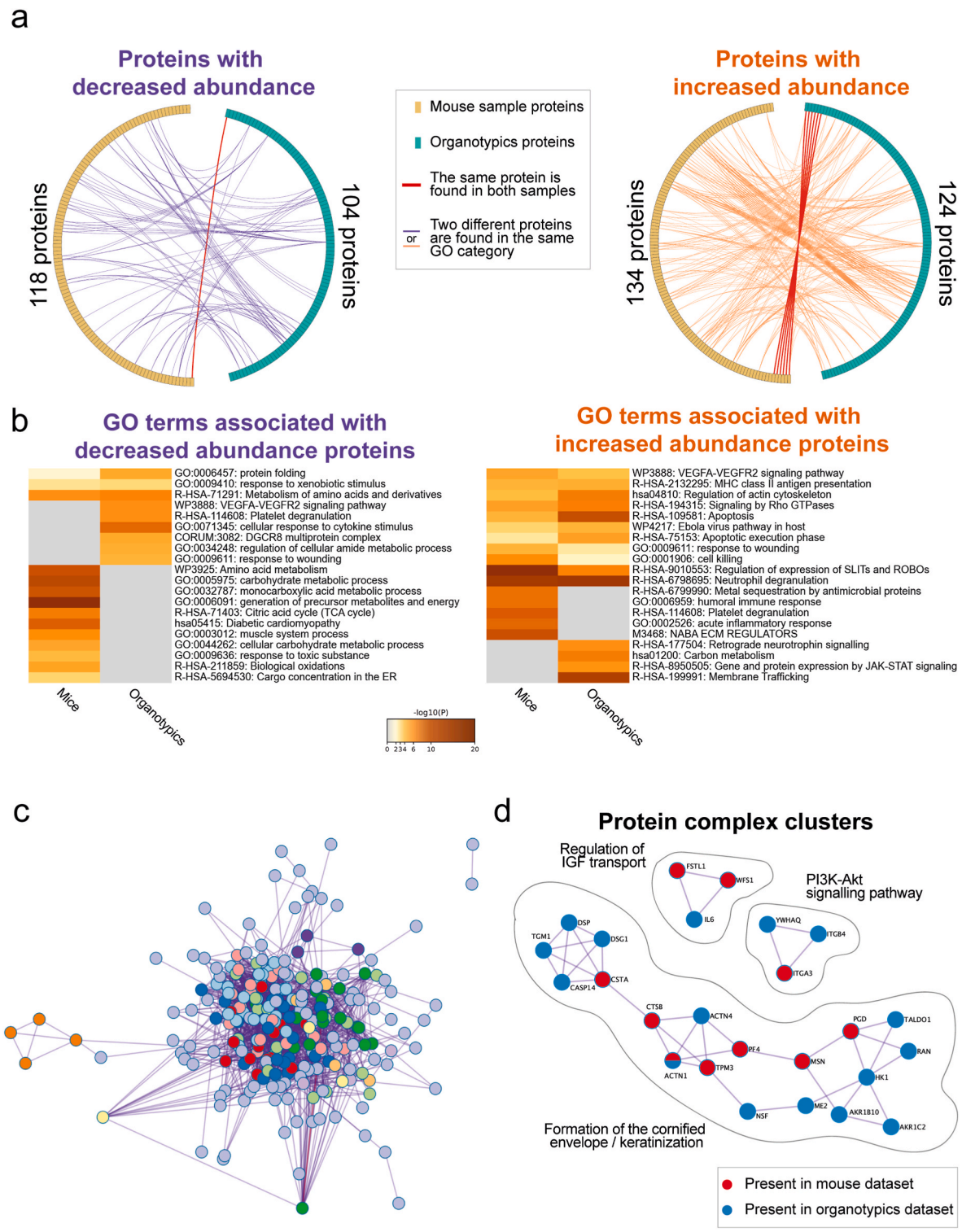

Fig. 4. Pathway enrichment analysis of significantly affected proteins in mouse and organotypic model samples upon exposure to *N. nigricollis* venom. **(a)** Circos plots depicting overlap between lists of proteins with decreased abundance (left) or increased abundance (right). Each line connects a protein from the mouse dataset (yellow blocks) to a protein from the organotypic model dataset (green blocks). Red lines connect identical proteins between the two datasets, whereas purple or orange lines (corresponding to decreased or increased abundance) connect proteins that are not identical, but which are both members of the same gene ontology terms. **(b)** Heatmap of the top 20 enriched gene ontology terms based on the lists of proteins with significantly decreased abundance (left) or increased abundance (right). The color-coding corresponds to each term's *p* value for either the mouse or organotypic model-derived dataset. **(c)** Complex interactome network based on the pooled collection of proteins with significantly increased abundance from both the mouse and organotypic model datasets. **(d)** Examples of extracted protein complexes and the enriched ontology terms associated with them. For interpretation of the references to color in this figure legend, the reader is referred to the Web version of this article.

the *in vivo* mouse model, especially in regard to the number of layers of epithelial cells. Mouse epidermis is comprised of a few layers of cells (Fig. 2a, right panel zoom-in), whereas human skin and the organotypic model used here display a higher number of layers in the epidermis (Fig. 2d). On the other hand, the extracellular matrix underlying the epithelial cell layer in the organotypic model only partially resembles the dermis, as it is rich in collagen and contains fibroblasts, but does not contain the typical skin appendages (sebaceous glands, hair follicles) present in mouse and human skin.

Our histological findings highlight pronounced differences in the morphology of normal and envenomed tissues in both models. In the case of mouse skin, the most prominent alteration observed was hyperplasia (Fig. 2b), corresponding to the re-epithelialization process that typically takes place after acute injury (Cañedo-Dorantes and Cañedo-Ayala, 2019). In a subset of the samples, more severe manifestations of necrosis could be seen, which was identified by the loss of epidermis altogether and the formation of proteinaceous material (Fig. 2c). In the case of the organotypic model, the effect of venom was more drastic, as it predominantly induced necrosis of epithelial cells and widespread disorganization of the epidermis. It is likely that a higher dose of venom, such as the one used previously by Rivel et al. (2016), would have induced a more widespread dermonecrotic effect in mice. The higher dose that was used in this study (63 μg) was determined by pilot unpublished dose-determination experiments and was selected so as to not surpass the maximum allowable lesion size outlined in the licensed animal experiment approval and to avoid any systemic signs of envenoming, which would have required early euthanasia of the animals. The lower dose (32 μg) injected in mice was similar to the dose that was administered to the organotypics.

The variable effects of the venom dosage in mice, which were observed on a histological level, were also reflected on a proteomics level. For example, we observed that the venom-subjected mouse replicate #2 clustered more closely with the control samples (Fig. 3b). Intriguingly, this is also the experimental animal that developed the largest lesion in response to the venom injection (Figure S1a). One plausible explanation for this discrepancy could be that the skin was so damaged in the lesion area that a lesser affected neighboring region was selected to make the slices for histology and proteomics. This clustering of a venom-subjected replicate with the controls may have important effects on the significance (*p* values) of the changes in abundance for some proteins in the mouse dataset. In conclusion, the damage induced in the organotypic models by the venom of *N. nigricollis* better resembles the severe pattern of dermonecrosis described in mice when using higher doses of venom, and is perhaps likely to simulate the ulceration and dermonecrosis observed in clinical cases of envenomings by *N. nigricollis* (World Health Organization, 2010), thus underscoring the potential utility of this model in the study of venom-induced skin damage.

Global proteomics analysis revealed a large overlap in identical proteins that made up the collective proteome in each of the two models (Fig. 3a). Compared to the organotypic models, which only have keratinocytes and fibroblasts present, additional cell types are present in the mouse dermis and hypodermis, such as mast cells, resident macrophages, dendritic cells, and endothelial cells (Joost et al., 2020). Additionally, venom treatment may cause the arrival and activation of leukocytes and macrophages, further expanding the repertoire of cell types present in the mouse skin (Koh and DiPietro, 2011), all of which likely result in the presence of proteins that are unique to the mouse-derived dataset. Further, a small subset of the differences in proteome consistency between the two models might be due to differential gene/protein nomenclature in humans and mice. Although most orthologs share the same gene symbol in mice and humans (the difference being that in mice the first letter of the gene symbol is uppercase and the rest are lowercase while in humans all letters are uppercase), there are still some instances of orthologous pairs maintaining different gene symbols and could impact their identification as being orthologous in our analysis (Wright and Bruford, 2006).

Many proteins whose abundance was significantly affected by the venom treatments were identified (Fig. 3c, Table S1 and S2). Although the number of identical proteins whose abundance was significantly affected in the datasets was quite low (Fig. 3d), pathway enrichment analysis highlighted a range of overlapping biological processes that correlate to proteins that are non-identical but are still somehow involved in those processes (Fig. 4a and b). Considering the important role that the cytoskeleton plays in wound healing responses, regulation of the actin cytoskeleton was, unsurprisingly, one of the terms found to be enriched in the pathway enrichment analysis (Abreu-Blanco et al., 2012). Signaling by Rho GTPases is another one of the top hits in the pathway enrichment analysis. Interestingly, constitutive activation of Rho GTPases was posited to underlie the toxicities of certain dermonecrosis-inducing bacterial toxins (Horiguchi, 2001). Although these toxins share no resemblance to the toxins present in the *N. nigricollis* venom, it is possible that the same signaling pathway might be impacted in this case too, but in a different way. Proteomic signs of apoptosis were also identified. This process is more strongly correlated to the organotypic model dataset, which is in agreement with the observation that epithelial cell damage was more pronounced in the histology of the organotypic models.

Some of the pathways highlighted by the pathway enrichment analysis were only present in one of the models and this observation can be explained by highlighting the differences between the two models. As mentioned above, venom exposure leads to immune cell infiltration of the skin in mice and therefore the mouse dataset was enriched for terms such as humoral immune response and acute inflammatory response (Fig. 4b, right). Such terms are not enriched in the organotypic model dataset since this model consists only of keratinocytes and fibroblasts. Additional indications of immune cell infiltration in the mouse skin are demonstrated by the abundance of chemokine/cytokine signaling molecules being increased in the mouse dataset, though not in a statistically significant manner (Figure S2a). It was also observed that DAMPs, molecules previously associated with viperid envenoming in mice (Rucavado et al., 2016), were more readily affected in our mouse dataset compared to that of the organotypic model (Figure S2a). It is unclear at this stage whether such differences between the models are solely due to the reduced complexity of the organotypic models, or whether some responses are more strongly correlated with a specific organism over another. More studies with higher number of replicates, and a range of venom dosages and exposure times would be necessary to better address the differences seen between the models at the proteome level.

When enriched terms that correlated with protein interactions between the combined pools of significantly affected proteins from both our datasets were examined, additional signaling pathways appeared (Fig. 4d). These included the IGF pathway and the PI3K/Akt signaling pathway, both of which are known to be involved in wound healing responses (Sadagurski et al., 2006; Teng et al., 2021). These findings further point towards the organotypic model recapitulating many of the established responses to skin tissue damage.

Certain facets of the experiments in this study were characterized by pronounced variability. Examples of this variability are the lesion area caused by the *N. nigricollis* venom in mice (Figure S1c), and the level of contraction of the collagen-fibroblast matrix of the organotypic models (Fig. 1b). Variability in the proteomics experiments, both inherent and technical, could perhaps explain to some extent why the organotypic models (which had 2 replicates as opposed to 3 in mice) had a higher number of significantly affected proteins compared to the total number of proteins detected compared to the mouse dataset (Fig. 3c). Such variability highlights the need to further characterize these models. Despite these limitations, our study underscored the potential value of the organotypic model to assess the action of dermonecrotic snake venoms and toxins.

In summary, we find that, in a number of promising ways, the organotypic model is able to recapitulate certain effects that *N. nigricollis* venom exerts in mice, both from a histological and a proteomic

perspective. Although only *N. nigricollis* venom was tested here as a proof of principle, we propose that this organotypic model can become a valuable tool in studying the effects of this and other locally-acting venoms. The introduction of this model complies with the 3Rs principle of replacing, reducing, and refining the use of animals in research (Gutiérrez et al., 2020), as it may eventually lead to the limitation of the current animal-based tests which cause pain and tissue damage. Until additional characterization studies have taken place to build on these early findings, we propose that this model is particularly well-suited to be used alongside (*i.e.* in parallel with) animal models, rather than to directly subsitute them. In the future, the approach employed here could potentially be further refined to find utility in the assessment of the efficacy of antivenoms, antibodies, and inhibitors against tissue-damaging toxins, as well as compounds with tissue regenerative effects, with the ultimate goal of developing more effective treatments for snakebite-induced dermonecrosis.

Ethical statement

All animal experiments were conducted using protocols approved by the Animal Welfare and Ethical Review Boards of the Liverpool School of Tropical Medicine and the University of Liverpool. The experiments were performed in specific pathogen-free conditions under licensed approval (PPL #P58464F90) of the UK Home Office and in accordance with the Animal [Scientific Procedures] Act 1986 and institutional guidance on animal care.

Author contributions statement

Shirin Ahmadi: Conceptualization, Formal Analysis, Funding Acquisition, Investigation, Methodology, Project Administration, Visualization, Writing - Original Draft Preparation, Writing - Review and Editing **Spyridon T. Pachis:** Formal Analysis, Project Administration, Visualization, Writing - Original Draft Preparation, Writing - Review and Editing **Konstantinos Kalogeropoulos:** Formal Analysis, Investigation, Writing - Review and Editing **Farrell McGeoghan:** Investigation, Methodology **Vahap Canbay:** Investigation **Steven R. Hall:** Investigation **Edouard P. Crittenden:** Investigation **Charlotte A. Dawson:** Investigation **Keirah E. Bartlett:** Investigation **José María Gutiérrez:** Writing - Review and Editing **Nicholas R. Casewell:** Resources, Writing - Review and Editing **Ulrich auf dem Keller:** Conceptualization, Funding Acquisition, Resources, Writing - Review and Editing **Andreas H. Laustsen**: Conceptualization, Funding Acquisition, Resources, Supervision, Writing - Review and Editing

Declaration of competing interest

The authors declare that they have no known competing financial interests or personal relationships that could have appeared to influence the work reported in this paper.

Data availability

Data will be made available on request.

Acknowledgements

This research was supported in part by a Young Investigator grant from the Villum Foundation (00025302) awarded to Andreas Laustsen. Shirin Ahmadi was additionally supported by the European Cooperation in Science and Technology (COST) through the action CA19144 EUVEN. Ulrich auf dem Keller acknowledges support by a Novo Nordisk Foundation Young Investigator Award (NNF16OC0020670), a project grant from LEO Foundation (LF-OC-19-000033) and an unrestricted research grant from Paul Hartmann AG.

Appendix A. Supplementary data

Supplementary data to this article can be found online at https://doi.org/10.1016/j.toxicon.2022.106955.

References

Abreu-Blanco, M.T., Watts, J.J., Verboon, J.M., Parkhurst, S.M., 2012. Cytoskeleton responses in wound repair. Cell. Mol. Life Sci. 69, 2469–2483. https://doi.org/10.1007/s00018-012-0928-2.

Aguilan, J.T., Kulej, K., Sidoli, S., 2020. Guide for protein fold change and p-value calculation for non-experts in proteomics. Mol Omics 16, 573–582. https://doi.org/10.1039/D0MO00087F.

Arnette, C., Koetsier, J.L., Hoover, P., Getsios, S., Green, K.J., 2016a. In vitro model of the epidermis: connecting protein function to 3D structure. Methods Enzymol. 569, 287–308. https://doi.org/10.1016/BS.MIE.2015.07.015.

Arnette, C., Koetsier, J.L., Hoover, P., Getsios, S., Green, K.J., 2016b. In vitro model of the epidermis: connecting protein function to 3D structure. Methods Enzymol. 569, 287–308. https://doi.org/10.1016/bs.mie.2015.07.015.

Cañedo-Dorantes, L., Cañedo-Ayala, M., 2019. Skin acute wound healing: a comprehensive Review. Int. J. Inflamm. 2019, 3706315 https://doi.org/10.1155/2019/3706315.

Chippaux, J.-P., 2010. [Guidelines for the production, control and regulation of snake antivenom immunoglobulins]. Biol Aujourdhui 204, 87–91. https://doi.org/10.1051/jbio/2009043.

Chippaux, J.-P., 2011. Estimate of the burden of snakebites in sub-Saharan Africa: a meta-analytic approach. Toxicon Off J Int Soc Toxinology 57, 586–599. https://doi.org/10.1016/j.toxicon.2010.12.022.

Chippaux, J.-P., 2017. Snakebite envenomation turns again into a neglected tropical disease. J. Venom. Anim. Toxins Incl. Trop. Dis. 23, 38. https://doi.org/10.1186/s40409-017-0127-6.

Choi, J., Lee, Y., Yoon, Y.J., Kim, C., Park, S., Kim, S., et al., 2019. Pimozide suppresses cancer cell migration and tumor metastasis through binding to ARPC2, a subunit of the Arp2/3 complex. Cancer Sci. 110, 3788–3801. https://doi.org/10.1111/cas.14205.

Dufton, M.J., Hider, R.C., 1988. Structure and pharmacology of elapid cytotoxins. Pharmacol. Ther. 36, 1–40. https://doi.org/10.1016/0163-7258(88)90111-8.

Dyring-Andersen, B., Løvendorf, M.B., Coscia, F., Santos, A., Møller, L.B.P., Colaço, A.R., et al., 2020. Spatially and cell-type resolved quantitative proteomic atlas of healthy human skin. Nat. Commun. 11, 5587. https://doi.org/10.1038/s41467-020-19383-8.

El-Ghalbzouri, A., Gibbs, S., Lamme, E., Van Blitterswijk, C.A., Ponec, M., 2002. Effect of fibroblasts on epidermal regeneration. Br. J. Dermatol. 147, 230–243. https://doi.org/10.1046/J.1365-2133.2002.04871.X.

Filipek, P.A., de Araujo, M.E.G., Vogel, G.F., De Smet, C.H., Eberharter, D., Rebsamen, M., et al., 2017. LAMTOR/Ragulator is a negative regulator of Arl8b- and BORC-dependent late endosomal positioning. J. Cell Biol. 216, 4199–4215. https://doi.org/10.1083/jcb.201703061.

Gutiérrez, J.M., León, G., Lomonte, B., Angulo, Y., 2011. Antivenoms for snakebite envenomings. Inflamm. Allergy - Drug Targets 10, 369–380. https://doi.org/10.2174/187152811797200669.

Gutiérrez, J.M., Calvete, J.J., Habib, A.G., Harrison, R.A., Williams, D.J., Warrell, D.A., 2017a. Snakebite envenoming. Nat. Rev. Dis. Prim. 31 (3), 1–21. https://doi.org/10.1038/nrdp.2017.63, 2017.

Gutiérrez, J.M., Solano, G., Pla, D., Herrera, M., Segura, Á., Vargas, M., et al., 2017b. Preclinical evaluation of the efficacy of antivenoms for snakebite envenoming: state-of-the-art and challenges ahead. Toxins 9, 163. https://doi.org/10.3390/toxins9050163.

Gutiérrez, J.M., Vargas, M., Segura, Á., Herrera, M., Villalta, M., Solano, G., et al., 2020. In vitro tests for assessing the neutralizing ability of snake antivenoms: toward the 3Rs principles. Front. Immunol. 11, 617429 https://doi.org/10.3389/fimmu.2020.617429.

Habib, A.G., 2013. Venomous snakes and snake envenomation in Nigeria. In: Gopalakrishnakone, P. (Ed.), Toxinology: Clinical Toxinology. Springer Netherlands, Dordrecht, pp. 1–21. https://doi.org/10.1007/978-94-007-6288-6_32-1.

Hamill, K.J., Hiroyasu, S., Colburn, Z.T., Ventrella, R.V., Hopkinson, S.B., Skalli, O., et al., 2015. Alpha actinin-1 regulates cell-matrix adhesion organization in keratinocytes: consequences for skin cell motility. J. Invest. Dermatol. 135, 1043–1052. https://doi.org/10.1038/jid.2014.505.

Ho, C.-H., Chiang, L.-C., Mao, Y.-C., Lan, K.-C., Tsai, S.-H., Shih, Y.-J., et al., 2021. Analysis of the necrosis-inducing components of the venom of Naja atra and assessment of the neutralization ability of freeze-dried antivenom. Toxins 13, 619. https://doi.org/10.3390/toxins13090619.

Horiguchi, Y., 2001. Escherichia coli cytotoxic necrotizing factors and Bordetella dermonecrotic toxin: the dermonecrosis-inducing toxins activating Rho small GTPases. Toxicon Off J Int Soc Toxinology 39, 1619–1627. https://doi.org/10.1016/s0041-0101(01)00149-0.

Joost, S., Annusver, K., Jacob, T., Sun, X., Dalessandri, T., Sivan, U., et al., 2020. The molecular anatomy of mouse skin during hair growth and rest. Cell Stem Cell 26, 441–457. https://doi.org/10.1016/j.stem.2020.01.012 e7.

Kessler, P., Marchot, P., Silva, M., Servent, D., 2017. The three-finger toxin fold: a multifunctional structural scaffold able to modulate cholinergic functions. J. Neurochem. 142 (Suppl. 2), 7–18. https://doi.org/10.1111/JNC.13975.

Koh, T.J., DiPietro, L.A., 2011. Inflammation and wound healing: the role of the macrophage. Expet Rev. Mol. Med. 13, e23. https://doi.org/10.1017/S1462399411001943.

Krieglstein, J., Lehmann, M., Mäurer, A., Gudermann, T., Pinkenburg, O., Wieland, T., et al., 2008. Reduced viability of neuronal cells after overexpression of protein histidine phosphatase. Neurochem. Int. 53, 132–136. https://doi.org/10.1016/j.neuint.2008.06.012.

Li, C., Luo, X., Zhao, S., Siu, G.K., Liang, Y., Chan, H.C., et al., 2017. COPI-TRAPPII activates Rab18 and regulates its lipid droplet association. EMBO J. 36, 441–457. https://doi.org/10.15252/embj.201694866.

Liu, C.-C., Chou, Y.-S., Chen, C.-Y., Liu, K.-L., Huang, G.-J., Yu, J.-S., et al., 2020. Pathogenesis of local necrosis induced by Naja atra venom: assessment of the neutralization ability of Taiwanese freeze-dried neurotoxic antivenom in animal models. PLoS Neglected Trop. Dis. 14, e0008054 https://doi.org/10.1371/journal.pntd.0008054.

Metsalu, T., Vilo, J., 2015. ClustVis: a web tool for visualizing clustering of multivariate data using Principal Component Analysis and heatmap. Nucleic Acids Res. 43, W566–W570. https://doi.org/10.1093/nar/gkv468.

Petras, D., Sanz, L., Segura, Á., Herrera, M., Villalta, M., Solano, D., et al., 2011. Snake venomics of African spitting cobras: toxin composition and assessment of congeneric cross-reactivity of the pan-African EchiTAb-Plus-ICP antivenom by antivenomics and neutralization approaches. J. Proteome Res. 10, 1266–1280. https://doi.org/10.1021/PR101040F.

Petrova, A., Celli, A., Jacquet, L., Dafou, D., Crumrine, D., Hupe, M., et al., 2014. 3D in vitro model of a functional epidermal permeability barrier from human embryonic stem cells and induced pluripotent stem cells. Stem Cell Rep. 2, 675–689. https://doi.org/10.1016/J.STEMCR.2014.03.009.

Preibisch, S., Saalfeld, S., Tomancak, P., 2009. Globally optimal stitching of tiled 3D microscopic image acquisitions. Bioinforma Oxf Engl 25, 1463–1465. https://doi.org/10.1093/bioinformatics/btp184.

Pucca, M.B., Ahmadi, S., Cerni, F.A., Ledsgaard, L., Sørensen, C.V., McGeoghan, F.T.S., et al., 2020. Unity makes strength: exploring intraspecies and interspecies toxin synergism between phospholipases A2 and cytotoxins. Front. Pharmacol. 11, 611. https://doi.org/10.3389/fphar.2020.00611.

Rivel, M., Solano, D., Herrera, M., Vargas, M., Villalta, M., Segura, Á., et al., 2016. Pathogenesis of dermonecrosis induced by venom of the spitting cobra, Naja nigricollis: an experimental study in mice. Toxicon 119, 171–179. https://doi.org/10.1016/j.toxicon.2016.06.006.

Rucavado, A., Nicolau, C.A., Escalante, T., Kim, J., Herrera, C., Gutiérrez, J.M., et al., 2016. Viperid envenomation wound exudate contributes to increased vascular permeability via a DAMPs/TLR-4 mediated pathway. Toxins 8, E349. https://doi.org/10.3390/toxins8120349.

Sadagurski, M., Yakar, S., Weingarten, G., Holzenberger, M., Rhodes, C.J., Breitkreutz, D., et al., 2006. Insulin-like growth factor 1 receptor signaling regulates skin development and inhibits skin keratinocyte differentiation. Mol. Cell Biol. 26, 2675–2687. https://doi.org/10.1128/MCB.26.7.2675-2687.2006.

Salgado, G., Ng, Y.Z., Koh, L.F., Goh, C.S.M., Common, J.E., 2017. Human reconstructed skin xenografts on mice to model skin physiology. Differentiation 98, 14–24. https://doi.org/10.1016/j.diff.2017.09.004.

Sancak, Y., Bar-Peled, L., Zoncu, R., Markhard, A.L., Nada, S., Sabatini, D.M., 2010. Ragulator-Rag complex targets mTORC1 to the lysosomal surface and is necessary for its activation by amino acids. Cell 141, 290–303. https://doi.org/10.1016/j.cell.2010.02.024.

Sanz-Gómez, N., Freije, A., Gandarillas, A., 2020. Keratinocyte differentiation by flow cytometry. Methods Mol Biol Clifton NJ 2109, 83–92. https://doi.org/10.1007/7651_2019_237.

Schindelin, J., Arganda-Carreras, I., Frise, E., Kaynig, V., Longair, M., Pietzsch, T., et al., 2012. Fiji: an open-source platform for biological-image analysis. Nat. Methods 9, 676–682. https://doi.org/10.1038/nmeth.2019.

Shannon, P., Markiel, A., Ozier, O., Baliga, N.S., Wang, J.T., Ramage, D., et al., 2003. Cytoscape: a software environment for integrated models of biomolecular interaction networks. Genome Res. 13, 2498–2504. https://doi.org/10.1101/gr.1239303.

Teng, Y., Fan, Y., Ma, J., Lu, W., Liu, N., Chen, Y., et al., 2021. The PI3K/akt pathway: emerging roles in skin homeostasis and a group of non-malignant skin disorders. Cells 10, 1219. https://doi.org/10.3390/cells10051219.

World Health Organization, 2010. Guidelines for the Prevention and Clinical Management of Snakebite in Africa.

Wright, M.W., Bruford, E.A., 2006. Human and orthologous gene nomenclature. Gene 369, 1–6. https://doi.org/10.1016/j.gene.2005.10.029.

Yousef, H., Alhajj, M., Sharma, S., 2021. Anatomy, Skin (Integument), Epidermis. StatPearls [cited 24 Jan 2022]. Available: https://www.ncbi.nlm.nih.gov/books/NBK470464/.

Zhao, Y., Huang, X., Zhang, Z., Zhang, Y., Zhang, G., Zan, T., et al., 2020. USP15 enhances Re-epithelialization through deubiquitinating EIF4A1 during cutaneous wound repair. Front. Cell Dev. Biol. 8, 529. https://doi.org/10.3389/fcell.2020.00529.

Zhou, Y., Zhou, B., Pache, L., Chang, M., Khodabakhshi, A.H., Tanaseichuk, O., et al., 2019. Metascape provides a biologist-oriented resource for the analysis of systems-level datasets. Nat. Commun. 10, 1523. https://doi.org/10.1038/s41467-019-09234-6.